Impact of Sr-Containing Secondary Phases on Oxide Conductivity in Solid-Oxide Electrolyzer Cells

Andrew J. E. Rowberg,[*,†] Heather Slomski,[‡,§] Namhoon Kim,[†] Nicholas A. Strange,[¶] Brian Gorman,[‡,§] Sarah Shulda,[‡] David S. Ginley,[‡] Kyoung E. Kweon,[*,†] and Brandon C. Wood[*,†]

[†]*Laboratory for Energy Applications for the Future (LEAF) and Quantum Simulations Group, Lawrence Livermore National Laboratory, Livermore, CA 94550, USA.*
[‡]*National Renewable Energy Laboratory, Golden, CO 80401, USA.*
[¶]*SLAC National Accelerator Laboratory, Menlo Park, CA 94025, USA.*
[§]*Colorado School of Mines, Golden, CO 80401, USA.*

E-mail: rowberg1@llnl.gov; kweon1@llnl.gov; wood37@llnl.gov

*Supporting Information (SI) for this article is given via a link at the end of the document.*

Abstract

Solid-oxide electrolyzer cells (SOECs) based on yttria-stabilized zirconia (YSZ) oxide electrolytes are devices capable of producing hydrogen with excess thermal energy. However, beginning with initial materials sintering and extending through electrochemical aging, Sr diffusion within the Gd-doped CeO_2 (GDC) barrier layer has been observed to lead to the formation of unwanted secondary phases such as SrO and $SrZrO_3$. To establish the impact of these phases on SOEC performance, we perform first-principles calculations to determine secondary phase bulk oxide conductivities and compared them to that of the YSZ electrolyte. We find that SrO has a low conductivity arising from poor mobility and a low concentration of oxygen vacancies (V_O^{2+}), and its presence in SOECs should therefore be avoided as much as possible. $SrZrO_3$ also has a lower oxide conductivity than YSZ; however, this discrepancy is primarily due to lower V_O^{2+} concentrations, not V_O^{2+} mobility. We find Y-doping to be a viable strategy to increase V_O^{2+} concentrations in $SrZrO_3$, with 16% substitution of Y on the Zr site leading to an ionic conductivity on par with that of YSZ. Energy dispersive x-ray spectroscopy obtained using scanning transmission electron microscopy on cross-sections of SOECs indicates that Y is the most common minority element present in $SrZrO_3$ forming near the GDC—YSZ interface. Thus, we expect $SrZrO_3$ to be rich in V_O^{2+} and not to hinder long-term device performance. These results from our combined computational–experimental analysis can inform future materials engineering strategies designed to limit the detrimental effects of Sr-induced secondary phase formation on SOEC performance.

Introduction

Electrolyzer cells are devices designed to convert water directly into molecular hydrogen via the reaction:

$$2H_2O \rightarrow 2H_2 + O_2. \qquad (1)$$
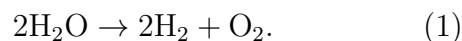
Central to the operation of an electrolyzer cell is the conduction of ionic species (protons, oxide ions, or hydronium ions) generated through the dissociation of H_2, O_2, and/or H_2O; simultaneously, electrical conductivity must be limited. Ionic conduction is mediated by an electrolyte, the choice of which depends largely on the temperature range of operation. For instance, polymer electrolyte membranes (PEMs) are widely used at low temperatures in PEM cells (50–80 °C), while solid oxides are preferred at high temperatures ($\sim$500°–900° C).[1] Solid oxide electrolytes, which can conduct either protons or oxide ions depending on the temperature and their crystal structure, form the basis of solid-oxide electrolyzer cells (SOECs). SOECs are particularly attractive due to their ability to use excess heat to convert water to steam and drive the electrolysis reaction, thereby reducing the demand for electricity relative to other electrolyzer cells and leading to their high inherent efficiency.[1–3]

A schematic of the typical SOEC architecture is shown in Fig. 1(a). The most common electrolyte in SOECs is yttria-stabilized zirconia (YSZ), which is one of the best oxide conductors known.[4] Porous metal oxides such as $La_{0.6}Sr_{0.4}Co_{0.2}Fe_{0.8}O_{3-\delta}$ (LSCF) are used as air electrodes in SOECs,[5–7] and Ni-YSZ ceramic-metal composites are typical choices for the fuel electrode.[6,8–10] These materials are selected for their mixed electronic and ionic conductivity and their durability. YSZ is separated from the air electrode by a Gd-doped CeO_2 (GDC) barrier layer, which conducts oxygen well but is primarily intended to limit the diffusion of cations from LSCF.[11–13] Nonetheless, due to the high operating temperatures, the diffusion of Sr atoms through the GDC layer is regularly observed during layer synthesis and device testing.[14–17] This diffusion leads to the formation of Sr-containing secondary phases, beginning with SrO, which initially precipitates at the LSCF—GDC interface.[18–21] Over time, SrO can migrate through the GDC barrier layer toward the GDC—YSZ interface, where $SrZrO_3$ (SZO) is often observed to form.[17,22–27]

Conclusions differ as to the long-term impacts of these phases on device performance.

SrO has not traditionally been linked to depressed ionic conductivity in SOECs, although it may interfere with oxygen reactivity.[28–30] As for SZO, some studies point to its lower oxide conductivity as one reason it may degrade performance.[17,22,31–33] However, another study showed that bulk SZO has at worst a neutral effect on SOEC performance, and that insofar as it inhibits oxide conductivity, the effect is due to resistive losses at grain boundaries and interfaces.[25]

Here, to elucidate the roles of bulk SrO and SZO on SOEC device performance, we analyze both materials alongside the YSZ electrolyte. These materials are each illustrated schematically in Fig. 1(b–e). We use first-principles calculations based on density functional theory (DFT)[34,35] with a hybrid exchange-correlation functional to study the oxide ion mobility, defect concentrations, and ionic conductivity of these three materials. We find that SrO has an extremely low ionic conductivity that cannot readily be improved; as such, it will be important to limit its presence in devices. SZO also has a lower oxide conductivity than YSZ, largely due to a smaller concentration of mobile oxygen vacancies (V_O). However, we find that this vacancy concentration can be tuned through atomic substitution. Specifically, introducing Y in SZO raises V_O concentrations by several orders of magnitude; with a sufficiently high Y content, the oxide ion conductivity in SZO will reach parity with that of YSZ.

In conjunction with our calculations, we also examine the chemistry of SOECs near the GDC—YSZ interface after 1000 hours of testing at 750 °C. Using energy dispersive x-ray spectroscopy maps obtained via scanning transmission electron microscopy (STEM-EDS), we observe the presence of large SZO precipitates accompanied by noticeable amounts of Y. As such, it appears that Y will readily diffuse from the YSZ layer into SZO, raising its ionic conductivity. By comparison, we find SrO to be much more dispersed, which should limit its detrimental impact. However, further studies should be conducted to ensure that SrO does not grow into thick, continuous layers over more extended periods of testing or under different

2

operating conditions. Notably, Department of Energy targets for high-temperature electrolysis include an ultimate lifetime goal of ~80,000 hours,[36] and our testing conditions may not be sufficiently long to investigate all effects that may occur under such long time scales.

Computational Methods

We conduct first-principles calculations based on density functional theory (DFT)[34,35] using the Heyd, Scuseria, and Ernzerhof (HSE06)[37,38] screened hybrid functional, as implemented in the Vienna *Ab initio* Simulation Package (VASP).[39] Using this hybrid functional, in which the short-range exchange potential is calculated by mixing a fraction of non-local Hartree-Fock exchange with the Perdew-Burke-Ernzerhof generalized gradient approximation (PBE-GGA),[40] ensures a reliable description of the electronic structure and the properties of point defects. The mixing parameter, which corresponds to the fraction of Hartree-Fock exchange, is tuned to reproduce experimentally determined band gaps; our choices are $\alpha = 0.44$ for SrO and $\alpha = 0.34$ for YSZ. For SZO, because there is disagreement as to the experimental band gap, we use the default mixing parameter $\alpha = 0.25$, which agrees with work from prior computational studies.[41–44] An $8\times8\times8$ **k**-point mesh is used to converge the cubic unit cells of SrO (eight atoms, four formula units), ZrO_2 (twelve atoms, four formula units), and cubic SZO (five atoms, one formula unit); for orthorhombic SZO (twenty atoms, four formula units), a $4\times4\times3$ **k**-point mesh is used. Total energies are converged to within 10^{-5} eV, and forces were considered converged when below 10 meV/Å. We use an energy cutoff of 500 eV for the plane-wave basis set, and the core electrons are described with projector-augmented-wave potentials,[45,46] with the Sr $4s^2$ $4p^6$ $5s^2$, Y $4s^2$ $4p^6$ $5s^2$ $4d^1$, Zr $4s^2$ $4p^6$ $5s^2$ $4d^2$, Ce $5s^2$ $5d^6$ $6s^2$ $5d^1$ $4f^1$, La $5s^2$ $5d^6$ $6s^2$ $5d^1$, Gd $5p^6$ $6s^2$ $5d^1$, and O $2s^2$ $2p^4$ electrons treated as valence. Note that the $4f$ electrons for Gd are treated as core states in order to reproduce the +3 oxidation state: this treatment has been shown to

yield accurate results for calculations of GDC,[47] and we find that it also reproduces the enthalpy of formation of Gd_2O_3. Structural images were generated with the VESTA3 software.[48]

Formation energies of point defects are calculated using supercells. For SrO, we construct a $2 \times 2 \times 2$ supercell of the conventional 8-atom cubic unit cell, containing 64 atoms. For SZO, having a 20-atom unit cell, we also construct a $2 \times 2 \times 2$ supercell, containing 160 atoms. Our YSZ structure is based on a $2 \times 2 \times 2$ supercell of the 12-atom cubic ZrO_2 unit cell, which contains 96 atoms prior to introducing Y and V_O. Supercell calculations are conducted using a single special **k** point at (0.25, 0.25, 0.25). For defect migration, we use the nudged elastic band (NEB) method with climbing images[49,50] and three intermediate images. NEB calculations are performed using the PBE-GGA functional for computational efficiency. For NEB calculations in GDC, a U correction of 5 eV is applied to the Ce $4f$ orbitals.

Defect Formation Energy

We calculate the formation energy $E^f(D^q)$ of a defect D in charge state q as:[51]

$$E^f(D^q) = E(D^q) - E_{\text{bulk}} + \sum n_A \mu_A + qE_F + \Delta_{\text{corr}}. \tag{2}$$

$E(D^q)$ is the total energy of a supercell containing D^q; E_{bulk} is the total energy of the defect-free supercell; n_A is the number of atoms of species A added ($n_A < 0$) or removed ($n_A > 0$) to create D^q; μ_A is the chemical potential of A; E_F is the position of the Fermi level relative to the valence band maximum (VBM); and Δ_{corr} is a finite-size correction term.[52,53] The formation energy is related to the defect concentration c via a Boltzmann relation:

$$c = N_{\text{sites}} \exp\left(-\frac{E^f}{k_B T}\right), \tag{3}$$

where N_{sites} is the site concentration of the defect, and k_B is Boltzmann's constant. It follows that lower formation energies correspond to exponentially higher defect concentrations. Initially, we treat E_F as an independent vari-
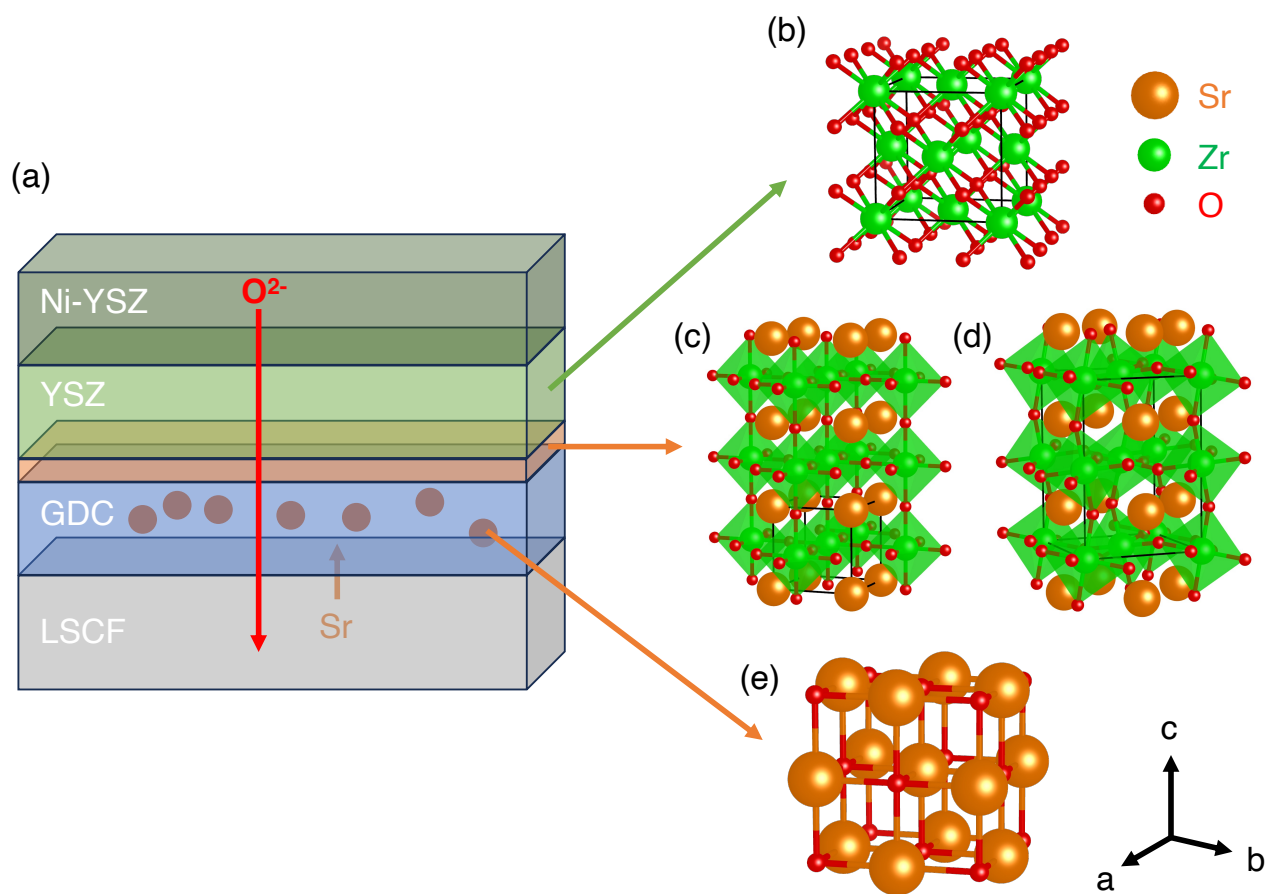
3

Figure 1: (a) A schematic of the key components of a solid-oxide electrolyzer cell. For components relevant to the work at hand, crystal structures are shown: (b) cubic ZrO_2, the structural basis for YSZ; (c) $SrZrO_3$ in its cubic phase, with the unit cell doubled in size along the **c** axis; (d) $SrZrO_3$ in its orthorhombic phase; (e) SrO.

able in calculating formation energies, meaning that plots of E^f vs. E_F will show each defect as lines with slopes q, with changes in slope corresponding to changes in the preferred charge state. However, the actual position of E_F in devices will be pinned by charge neutrality, which is determined in insulators by the position where the lines corresponding to the lowest energy positively and negatively charged defects intersect.

The chemical potentials μ_A reflect the energetic preference for specific elements under chosen conditions. We define these values based on their deviation $\Delta\mu_A$ from a reference energy as:

$$\mu_A = E_A + \Delta\mu_A, \qquad (4)$$

where E_A is the total energy of the elemental reference structure, i.e., the ground-state structures of Y (hcp), Zr (hcp), or Sr (fcc) metals, or an O atom in molecular O_2. To prevent the precipitation of these elemental phases, we require that $\Delta\mu_A \leq 0$ for each element A.

We assume conditions corresponding to thermodynamic equilibrium, which is captured by the following expression for the case of SrO:

$$\Delta\mu_{Sr} + \Delta\mu_O = \Delta H^f(SrO), \qquad (5)$$

where $\Delta H^f(SrO)$ is the enthalpy of formation of SrO. We can explore variations in the SrO chemistry by varying the chemical potentials from the Sr-rich limit [$\Delta\mu_{Sr} = 0$, $\Delta\mu_O = \Delta H^f(SrO)$] to the O-rich limit [$\Delta\mu_{Sr} = \Delta H^f(SrO)$, $\Delta\mu_O = 0$]. These limits are illustrated on a line corresponding to SrO in Fig. 2.

Similarly, for SZO to be thermodynamically stable:

$$\Delta\mu_{Sr} + \Delta\mu_{Zr} + 3\Delta\mu_O = \Delta H^f(SrZrO_3). \qquad (6)$$

For YSZ, having a concentration $Y_x Zr_{1-x} O_{2-x/2}$, the equivalent condition is:

$$x\Delta\mu_Y + (1-x)\Delta\mu_{Zr} + (2-x/2)\Delta\mu_O = \Delta H^f(YSZ). \qquad (7)$$

For both of these ternary compounds, additional bounds are placed on the chemical potentials by requiring that limiting phases do not precipitate. Taking SZO as an example, for Sr,
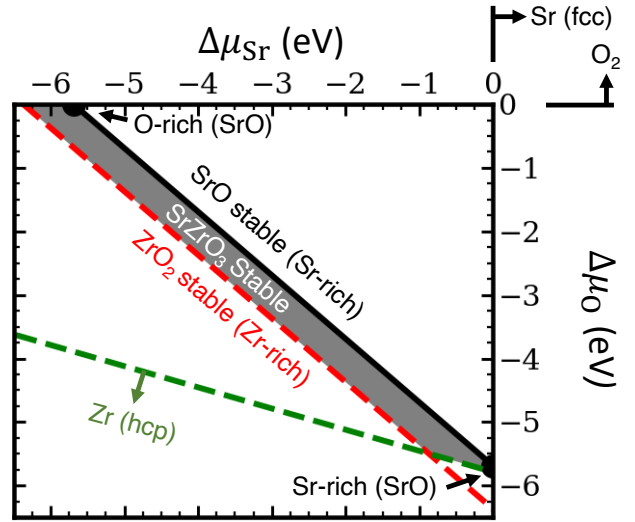

Figure 2: Chemical potential phase stability diagram for $SrZrO_3$ and SrO, plotted as $\Delta\mu_{Sr}$ vs. $\Delta\mu_O$. The (2D) stability region for $SrZrO_3$ is shaded gray, while the (1D) stability region for SrO is plotted as a thick black line. The stability lines of ZrO_2 and SrO correspond to Zr-rich and Sr-rich limits for $SrZrO_3$. O-rich and Sr-rich limits are also labeled for SrO. Lines and arrows are also used to indicate where elemental Sr, Zr, and O_2 phases become thermodynamically preferred.

this condition is expressed as:

$$\Delta\mu_{Sr} + \Delta\mu_O \leq \Delta H^f(SrO). \qquad (8)$$

And for Zr:

$$\Delta\mu_{Zr} + 2\Delta\mu_O \leq \Delta H^f(ZrO_2). \qquad (9)$$

Based on eq 6 and the upper limit of eq 8, we can define "Sr-rich" conditions (equivalently, "Zr-poor") as those for which $\Delta\mu_{Sr}$ is maximized while preventing precipitation of SrO or Sr metal. Similarly, eqs 6 and 9 allow us to define "Zr-rich" ("Sr-poor") conditions, where $\Delta\mu_{Zr}$ is maximized while ensuring that ZrO_2 does not precipitate. Again, these limits can be visualized in Fig. 2, where stability of SZO corresponds to the shaded region.

We can treat impurities similarly. For example, to calculate Y impurities in SrO (e.g., Y_{Sr}^+), we ensure that Y_2O_3 will not precipitate by requiring that it is not thermodynamically stable:

$$2\Delta\mu_Y + 3\Delta\mu_O \leq \Delta H^f(Y_2O_3). \qquad (10)$$

For simplicity, we present impurity formation energies at the solubility limit of impurity phases, corresponding to the upper limit of the inequality above.

Defect Concentrations

Using eq 3, we can identify how defect concentrations change under different operating conditions. Specifically, by enforcing charge neutrality among all the defects we calculate, we can determine the concentrations for each species and the position of the Fermi level for a given set of chemical potentials. This procedure requires two additional parameters, namely, the electron and hole concentrations. We determine electron concentrations by integrating the calculated density of states (DOS) near the conduction band minimum (CBM), using the expression:[54]

$$n = \int_{E_{CBM}}^{\infty} g_C(E)f(E)dE \qquad (11)$$

where $g_C(E)$ is the conduction band DOS and $f(E)$ is the Fermi-Dirac occupation function. Similarly, for holes, we determine the carrier concentration by integrating the DOS near the VBM:

$$p = \int_{-\infty}^{E_{VBM}} g_V(E)[1 - f(E)]dE , \qquad (12)$$

where $g_V(E)$ is the valence band DOS.

We can then plot defect and carrier concentrations as a function of $\Delta\mu_O$, requiring calculations of defect equilibrium at each value of $\Delta\mu_O$ in the ranges we present. These values of $\Delta\mu_O$ are connected to experimentally measurable temperatures and partial pressures using the expression:

$$2\Delta\mu_O = H^0(T) - TS^0(T) + RT\ln\frac{P_{O_2}}{P^0}, \quad (13)$$

where $H^0(T)$ and $S^0(T)$ are thermodynamic values tabulated for O_2,[55] P_{O_2} is the partial pressure, and P^0 is the pressure at the standard conditions used in the tabulation.

Results and Discussion

Bulk Properties

We begin by calculating bulk properties for YSZ, SrO, and SZO, which we list in Table 1 alongside experimental values. For YSZ, SrO, and cubic SZO, we also list the lattice parameters extracted from our XRD analysis of SOECs after 1000 hours of testing [Fig. S1]. For orthorhombic SZO, which is not observed in our SOECs, we list lattice parameters from the literature. The agreement is very good in each case.

Note that, for SZO, we consider two phases: the cubic perovskite [c-SrZrO$_3$, Fig. 1(c)] and the orthorhombic perovskite [o-SrZrO$_3$, Fig. 1(d)]. When it forms in SOECs, SZO is often assumed to adopt the cubic structure, although we note that our computed XRD analysis [Fig. S1(c)] indicate that both phases have similar diffraction patterns, and it may therefore be difficult to distinguish them. While the cubic transition temperature has been mea-

Table 1: Calculated and reported bulk properties of materials under investigation in our study.

compound	Calculated				Experimental			
	a (Å)	b (Å)	c (Å)	E_g (eV)	a (Å)	b (Å)	c (Å)	E_g (eV)
YSZ	5.14	5.14	5.15	6.13	5.13	–	–	6.1[56]
SrO	5.14	–	–	5.97	5.08	–	–	5.90[57]
c-SrZrO$_3$	4.14	–	–	4.88	4.11	–	–	–
o-SrZrO$_3$	5.78	5.84	8.20	5.34	5.80[58]	5.82[58]	8.21[58]	5.2,[59] 5.6[60]

sured to be $\sim$1360–1443 K,[58,61,62] it is possible that it may be stabilized at the GDC—YSZ boundary at lower temperatures due to strain or other interfacial effects. The cubic phase is dynamically unstable at 0 K relative to the ground-state orthorhombic phase; as such, it is not feasible to calculate defect formation energies in the cubic phase using DFT, and we therefore use the orthorhombic phase as a proxy for cubic SZO throughout our discussion. In the supporting information (SI), we justify this decision by showing that V_O^0 formation energies are unaffected by the choice of initial structure using finite temperature *ab initio* molecular dynamics (AIMD) simulations [Fig. S2].

For YSZ, our structure is based on the high-temperature cubic fluorite phase of ZrO$_2$, which is unstable even at typical SOEC operating temperatures. However, the substitution of small amounts of Y for Zr stabilizes the cubic phase, while also reducing the oxygen content in order to maintain charge balance. Typical compositions of YSZ contain $\sim$8–10 mol% Y$_2$O$_3$ ($\sim$16–20 mol% Y).[63–65] Following a previous computational study,[66] we construct our YSZ cells with the stoichiometry Y$_6$Zr$_{26}$O$_{61}$, which corresponds to $\sim$9 mol% Y$_2$O$_3$. We examined 29 structures based on this stoichiometry and selected the lowest-energy structure for subsequent calculations of YSZ. The structure is slightly off-cubic, as evidenced by the slight discrepancy among lattice parameters reported in Table 1. More details are provided in the SI.

We also calculate enthalpies of formation for the four compounds under investigation here and several relevant limiting phases, which we list in Table 2. These include monoclincic ZrO$_2$, CeO$_2$, Gd$_2$O$_3$, La$_2$O$_3$, and Y$_2$O$_3$, the latter four

of which are relevant to our calculations of impurity incorporation. In general, our calculated values compare well with experimental enthalpies where available. We are unaware of experimental enthalpies of formation for YSZ and cubic SZO. In the case of YSZ, our calculated ΔH^f is similar to that of ZrO$_2$, which is unsurprising in light of their chemical similarities. For cubic SZO, our calculated ΔH^f agrees well with that of a previous computational work (–17.15 eV) using the same exchange-correlation functional.[41]

Oxygen Diffusivity

We begin our analysis of oxygen conductivity by computing energetic barriers for V_O migration in SrO, SZO, and YSZ using the NEB method. These barriers are directly related to diffusivity by the expression:

$$D(T) = D_0 \exp\left(-\frac{E_b}{k_B T}\right), \qquad (14)$$

where E_b is the migration barrier. The prefactor D_0 is given by

$$D_0 \approx \alpha \nu a^2 \exp\left(\frac{\Delta S}{k_B}\right). \qquad (15)$$

Here, α is a geometry-related factor that is often close to unity; ν is a hopping frequency that can be approximated as 10^{13} s^{-1}, close to a typical phonon frequency; a is the distance between sites; and ΔS is an entropy term, which we assume here to be small.[70]

We compute migration barriers in each material for each possible charge state of V_O^q ($q = 0$, +1, and +2). Our results are summarized in

Table 2: Calculated and reported bulk properties of materials under investigation in our study.

compound	ΔH^f (eV per formula unit)	
	Calculated	Experimental
YSZ	–10.81	–
SrO	–5.69	–6.14[67]
c-SrZrO$_3$	–17.13	–
o-SrZrO$_3$	–17.36	–18.28[68]
ZrO$_2$	–10.99	–11.41[67]
CeO$_2$	–11.28	–11.29[67]
Gd$_2$O$_3$	–18.69	–18.86[69]
La$_2$O$_3$	–17.94	–18.59[67]
Y$_2$O$_3$	–18.92	–19.75[67]

Table 3. Both YSZ and SZO have multiple pathways for V_O migration, resulting in a range of barriers: in the case of SZO, this fact reflects the lower energy of V_O on the apical site compared to the planar sites in its orthorhombic structure, while for YSZ, the structure we examine is simply highly disordered (see Fig. S3 and surrounding discussion in SI) and has a wide range of V_O formation energies leading to different migration barriers. In each case, as the charge state increases from 0 to +2, the migration barriers broadly decrease. This trend—and the specific values of the barriers—agree well with previous computational work examining V_O diffusion in SZO.[71]

Based on these results and eq 14, we compute the oxide ion diffusivities for each material and plot our results in Fig. 3, assuming V_O to be in its most common charge state, $q = +2$. Also shown are schematic illustrations of the pathways for V_O migration in each material. It is clear that SrO stands out due its low diffusivity. On the other hand, the range of diffusivities for SZO falls within that of YSZ, suggesting that the diffusivity of SZO is not a limiting factor when it is present in SOECs.

Defect Concentration

Native Defects

For a material to possess high ionic conductivity, it should have both a high diffusivity and a large concentration of the mobile species. To determine the V_O^{2+} concentrations in SrO and SZO, we compute defect formation energies in both materials.

Our calculated formation energies are plotted in Fig. 4. We begin with SrO. Under Sr-rich conditions [Fig. 4(a)], the Fermi level will be pinned close to the CBM by V_{Sr}^{2-} and V_O^+; however, the most prominent defect at these conditions will be V_O^0. As discussed in the previous section, V_O^0 is significantly less mobile than V_O^{2+}, so these conditions will not be advantageous for high oxide conductivity. Under O-rich conditions [Fig. 4(b)], the Fermi level will be pinned about 2 eV above the VBM by V_O^{2+} and V_{Sr}^-. However, the formation energy of V_O^{2+} at these conditions ($\sim$ 3 eV) is large and will lead to low defect concentrations.

The situation in SZO is more encouraging. Between Sr-rich [Fig. 4(c)] and Zr-rich [Fig. 4(d)] conditions, the Fermi level remains close to the middle of the band gap, where V_O will prefer the +2 charge state. However, formation energies will be large ($\sim$ 2 eV), meaning that their concentrations will be low. Furthermore, for Zr-rich conditions, V_O^{2+} will not be

8

Table 3: Calculated migration barriers for oxygen vacancies in the 0, +1, and +2 charge.

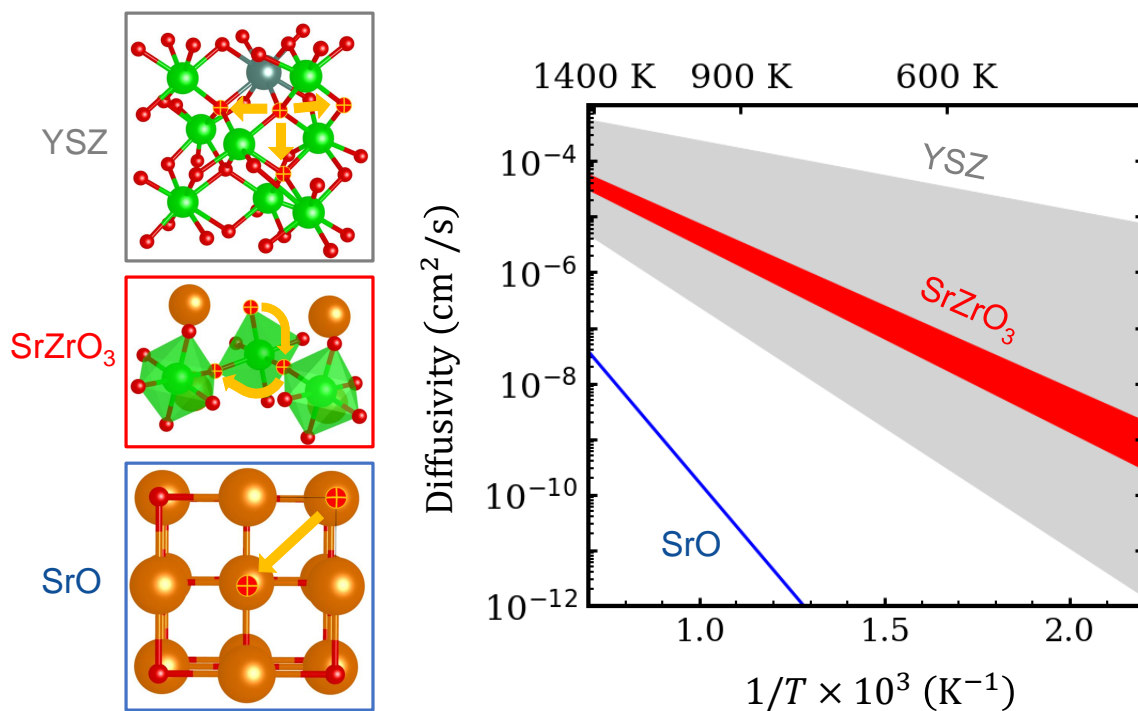| Compound	Migration Barrier (eV)		
	V_O^0	V_O^+	V_O^{2+}
YSZ	0.66–2.09	0.35–1.31	0.25–0.87
SrO	2.79	2.55	1.57
SrZrO$_3$	1.55–1.69	1.34–1.46	0.54–0.67

Figure 3: Calculated diffusivity of V_O^{2+} in YSZ, SrZrO$_3$, and SrO, using computed migration barriers. Schematic pathways for oxygen diffusion in each material are shown on the left.
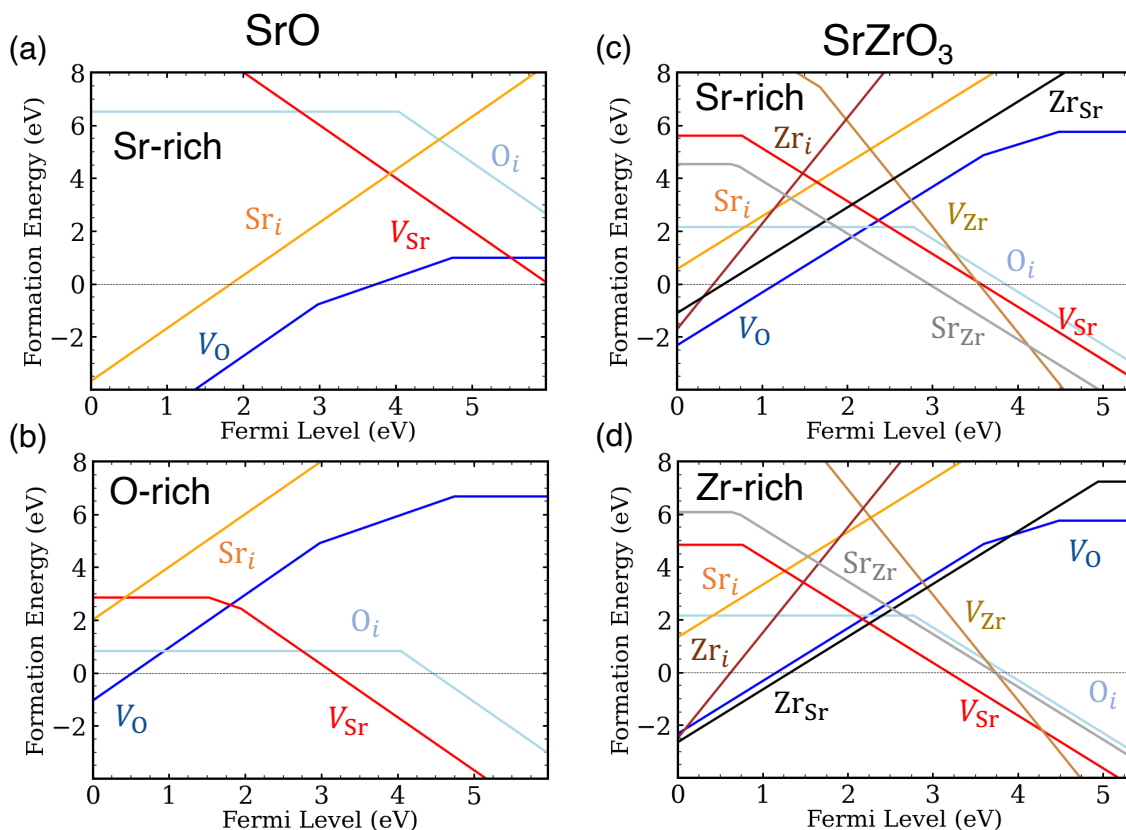
9

Figure 4: Calculated defect formation energies in SrO under (a) Sr-rich and (b) O-rich conditions, and in SrZrO$_3$ under (c) Sr-rich and (d) Zr-rich conditions. For SrZrO$_3$, $\Delta\mu_O = -1.099$ eV, which corresponds to $P_{O_2} = 1$ atm at 1000 K. Sr-rich, O-rich, and Zr-rich conditions correspond to those illustrated in the chemical stability diagram in Fig. 2.

the lowest-energy donor defect: instead, cation antisites (specifically, Zr_{Sr}^{2+}) will have slightly lower formation energies. These results suggest that Sr-rich conditions are most optimal for high oxide conductivity. Assuming that SZO precipitates from Sr-rich particulates passing toward the GDC—YSZ interface, we believe that it is reasonable to assume that Sr-rich conditions are most relevant, particularly at early stages of SZO growth. Unless otherwise stated, we will therefore focus on Sr-rich conditions for the remainder of our discussion.

Impurities

It is well established that doping SZO and chemically similar perovskite oxides with a trivalent element (e.g., Sc, Y, Yb) can significantly boost V_O^{2+} concentrations.[72] A similar strategy may therefore benefit oxide ion conductivity in SZO. Notably, there are several cations present in other components of the SOEC that may incorporate in SZO during its formation and increase V_O^{2+} concentrations. Among these, we consider four here: Ce, Gd, La, and Y. Ce and Gd are both present in GDC; La is present in LSCF and may diffuse through GDC along with Sr; and Y may accompany any Zr that leaves the YSZ electrolyte to form SZO.

We calculate the formation energies of these dopant species for SrO [Fig. S4] and SZO [Figs. S5 and S6], considering substitution on the Sr site and, for SZO, the Zr site as well. Based on these results, we calculate the concentrations of defects and impurities in SrO [Fig. S7] and SZO [Figs. S8 and S9]. For ease of presentation, we plot V_O^{2+} concentrations by themselves for undoped and doped systems in Fig. 5. Interestingly, for SrO [Fig. 5(a)], doping will uniformly reduce the V_O^{2+} concentrations, which are low in the bulk material to begin. Each dopant will substitute on the Sr site as an electron donor, meaning that they will compete with V_O^{2+} formation.

On the other hand, for SZO [Fig. 5(b)], the impact on V_O^{2+} concentration depends on the specific dopant. Among the dopants we consider, Y raises V_O^{2+} concentrations, while Gd, La, and Ce reduce them (Gd only slightly).

This finding for Y is unsurprising, considering that it is one of the most popular dopants for introducing V_O^{2+} in perovskite oxides.[72] Y forms favorably on the Zr-site as Y_{Zr}^-, which will encourage V_O^{2+} formation. We note that Y_{Sr}^+ actually has a slightly lower formation energy than V_O^{2+} at the Fermi level position corresponding to charge neutrality; however, the energies of the two donor species are similar, meaning that V_O^{2+} formation will still be improved by Y doping. Conversely, Ce, Gd, and La are more favorable as donor species (Ce_{Sr}^{2+}, Gd_{Sr}^+ and La_{Sr}^+) than Y, meaning that they will compete more strongly with V_O^{2+} formation. This result for La agrees with a previous experimental study finding suppressed oxide conductivity in La-doped SZO due to preferential substitution on the Sr site.[73]

Cation Impurity Migration through GDC

We expect that Y will incorporate readily in SZO by accompanying Zr moving from YSZ during nucleation of the SZO phase. Indeed, Develos-Baraginao *et al.* demonstrated that this incorporation can occur and has a beneficial effect on oxide conductivity in bulk SZO.[25] Ce and Gd may also incorporate from the neighboring GDC barrier layer, while La would need to diffuse along with Sr from LSCF through the GDC layer.

To investigate the favorability of cation diffusion through the GDC layer, we perform additional NEB calculations for the four cations considered in this work. Specifically, we simulate cation diffusion as mediated by V_{Ce} in pure CeO_2 along the $\langle 110 \rangle$ direction, which has been shown previously to be the dominant pathway for cation diffusion.[74] We have confirmed that explicitly including Gd in our CeO_2 cells to model GDC has a negligible effect on our results (see Table S2 in the SI). As oxygen vacancies are formed in GDC as a direct consequence of Gd doping, we also consider pathways with a single V_O along the migration pathway. [See Fig. S10 for schematics of the pathways we consider.] In each of our calculations, we consider the most prevalent charge states of the impurities (Gd_{Ce}^-, La_{Ce}^-, and Sr_{Ce}^{2-}) and vacancies (V_O^{2+}
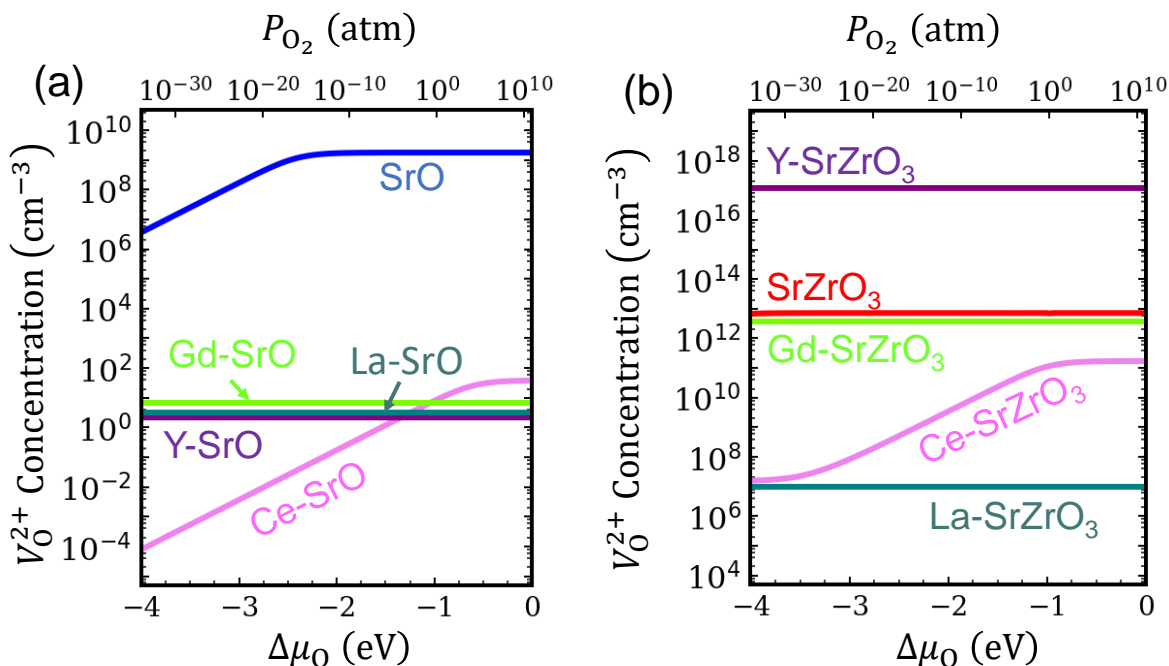
11

Figure 5: Concentrations of V_O^{2+} in (a) SrO and (b) SrZrO$_3$ (under Sr-rich conditions), both for undoped and doped systems, at $T = 1000$ K.

and V_{Ce}^{4-}).

Table 4: Calculated migration barriers (in eV) for cation impurities $I = \{Ce, Gd, La, Sr\}$ in CeO$_2$ moving to a nearby V_{Ce}^{4-}.

$I =$	Ce	Gd	La	Sr
I_{Ce}	4.76	5.26	4.47	3.67
$I_{Ce} + V_O^{2+}$	3.69	3.42	2.94	2.19

Our results are summarized in Table 4. The migration barriers for cation diffusion in CeO$_2$ are large, but they decrease by more than 1 eV when a V_O^{2+} is present along the migration path. Barriers are largest for Gd (without V_O) and Ce (with V_O), suggesting that these cations will diffuse relatively slowly; however, they are also immediately adjacent to the GDC—YSZ interface, so they may participate in interfacial reactions regardless. Our results for Ce diffusion agree well with prior computational studies.[74,75] La has significantly larger barriers than Sr (roughly 0.8 eV higher), suggesting that its diffusion through GDC will be much slower.

We can express our results another way by invoking transition state theory.[76] For a species

with migration barrier E_b, its hopping rate Γ can be expressed as:

$$\Gamma = \Gamma_0 \exp\left(-\frac{E_b}{k_B T}\right). \qquad (16)$$

Here, Γ_0 is a prefactor typically on the order of 10^{14} s^{-1}. We can approximate the temperature at which a species becomes mobile by solving for T when $\Gamma = 1$ s^{-1}, providing a reasonable metric for assessing relative mobilities. Considering the prevalence of V_O in GDC, we focus on barriers with V_O present along the migration pathway. By this metric, only Sr will be mobile at temperatures characteristic of SOEC operation ($\sim$1000 K), as it becomes mobile around 788 K. La impurities are mobile around 1060 K (close to temperatures of interest), Gd at 1230 K, and Ce at 1300 K. These temperatures may be reached during sintering, particularly for La; otherwise, each of these species will be relatively stationary.

There are other factors that may lead to cation diffusion through the GDC barrier layer. As mentioned, Ce and Gd diffusion should not be discounted, as they are present in GDC and

12

therefore immediately adjacent to SZO when it nucleates. Importantly, the long operating times of these devices mean that even energetically unfavorable migration pathways may eventually lead to measurable levels of impurity contamination. Additional diffusion pathways may also be relevant, including diffusion across grain boundaries and surfaces, which we do not consider here. Surface diffusion in particular is a subject we will investigate in future work.

Estimating Oxide Conductivity

We can couple our results for V_O^{2+} diffusivity and concentration to estimate the oxide conductivity in SrO and SZO under different doping conditions. Ionic conductivity depends on both the formation energy of mobile charge carriers as well as their migration barrier. These two quantities can be related to conductivity via the Nernst-Einstein equation:[77]

$$\sigma = \frac{cDe^2}{k_BT} = \frac{D_0e^2N_{\text{sites}}}{k_BT}\exp\left(-\frac{(E^f+E_b)}{k_BT}\right). \tag{17}$$

Note that the sum $E^f + E_b$ is the activation energy. In order to report a total ionic conductivity, we add the individual contributions from each V_O migration pathway reflected in the range of diffusivities shown for YSZ and SZO in Fig. 3, using the pertinent values for E^f and E_b for the different V_O^{2+} configurations.

Our calculated conductivities are plotted in Fig. 6. For YSZ, we use concentrations of V_O^{2+} based on calculated formation energies [Fig. S11]. As expected, the conductivity of SrO is very low, while that of bulk SZO is higher but still considerably less than that of YSZ.

Following from our discussion of doping in the previous section, Y-doped SZO has a significantly higher conductivity, following from its higher V_O^{2+} concentrations. At our calculated solubility limit of Y_2O_3, the Y concentration of SZO corresponds to a composition of $Sr(Zr_{0.91}Y_{0.09})O_{3-\delta}$, for which the oxide conductivity is a few orders of magnitude lower than that of YSZ at typical operating temperatures. However, higher experimental concen-

trations have been reported, including a composition of $Sr(Zr_{0.84}Y_{0.16})O_{3-\delta}$ by Labrincha et al.[78] This composition may be achievable under non-equilibrium conditions typical of SOEC operation, and as such, we include it as an upper limit for Y incorporation. Such high levels of Y doping lead to oxide conductivities almost identical to those we calculate for YSZ.
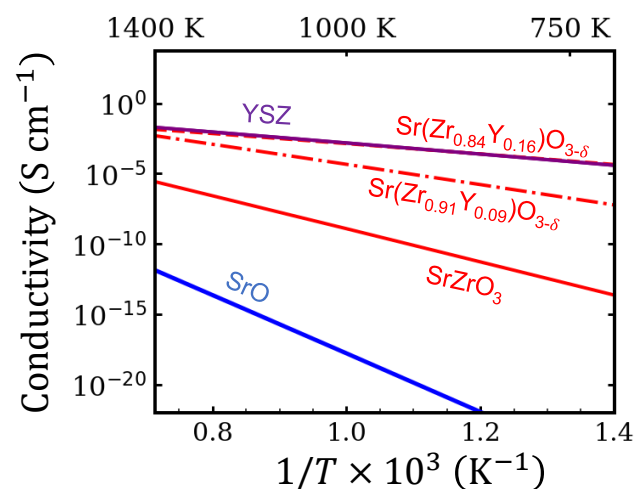

Figure 6: Oxide ionic conductivities for YSZ, SrO, and doped and undoped SrZrO$_3$, estimated using eq 17.

Labrincha et al. reported the high-temperature conductivity of bulk and Y-doped SZO [$Sr(Zr_{0.84}Y_{0.16})O_{3-\delta}$], allowing us to validate our results.[78] For bulk SZO, they reported a total conductivity of 3.5×10^{-5} S cm^{-1} at 1176 K, and 5.3×10^{-5} S cm^{-1} at 1389 K. For comparison, we estimate oxide conductivities of 1.1×10^{-7} S cm^{-1} at 1200 K, and 2.7×10^{-6} S cm^{-1} at 1400 K. These experimentally measured conductivities are likely higher than those we predict due to contributions from protonic and electrical conductivity, which we do not consider. Experimental results for the Y-doped samples specifically extracted the oxide conductivity, reporting 1.5×10^{-4} S cm^{-1} at 1075 K and 1.1×10^{-3} S cm^{-1} at 1389 K. Our calculated conductivities for Y-doped SZO ($Zr_{0.84}Y_{0.16}$) are very close to these values: 2.0×10^{-4} S cm^{-1} at 1100 K, and 5.0×10^{-3} S cm^{-1} at 1400 K.

Our calculations for YSZ are also consistent with experimental measurements. For a

13

single-crystal YSZ sample with approximately the same Y content as that which we assume here, Ahamer *et al.* reported conductivities of approximately 3.4×10^{-3} S cm^{-1} at 1000 K, 4.7×10^{-3} S cm^{-1} at 1100 K, and 5.8×10^{-3} S cm^{-1} at 1200 K.[79] By comparison, we calculate conductivities of 1.5×10^{-3} S cm^{-1} at 1000 K, 3.4×10^{-3} S cm^{-1} at 1100 K, and 6.8×10^{-3} S cm^{-1} at 1200 K, in each case close to experimental measurements.

Experimental Analysis

To develop a clearer picture of where SrO and SZO are likely to be present in SOECs, as well as the likelihood of impurity elements forming within them, we examine the chemical signatures of STEM-EDS maps of SOECs after 1000 hours of testing [details regarding the methodology are provided in the SI]. We focus on the GDC—YSZ interface, where SZO is expected to form.

Our STEM-EDS images are shown in Fig. 7, for which elemental signals of Sr and Zr are depicted. We focus on four distinct regions containing Sr, ranging spatially from the GDC interior to the GDC—YSZ interface. Elemental analysis of these regions is provided in Table S3 in the SI, although we note that our measured atomic percentages have large error bars, and oxygen is not included in the analysis due to difficulties with its detection.

The region deepest in the GDC layer (region 1) contains small, scattered amounts of Sr (19 ± 8 at%) within the GDC matrix, which are not accompanied by Zr (4 ± 2 at%) and thus suggest the presence of disperse SrO particles. In region 2, closer to the interface, a larger Zr signal (31 ± 10 at%) accompanies Sr (35 ± 11 at%) with a similar concentration, suggesting the presence of SZO. In regions 3 and 4, SZO also appears to be present, albeit accompanied by GDC in region 3.

We do not plot the Y signal in Fig. 7, as it tends to overlap significantly with Zr and is difficult to discern by eye. However, we have quantified Y concentrations in several regions of interest [Table S3]. Critically, the regions in Fig. 7 that we expect to contain SZO (2, 3, and

4) also contain noticeable concentrations of Y (11 ± 1 at% in region 2; 7 ± 2 at% in region 3; and 12 ± 2 at% in region 4). In each case, the atomic concentration of Y is on the order of one-third that of Sr and Zr. Concentrations of Ce and Gd are also high in regions 2 (19 ± 7 at% Ce and 4 ± 2 at% Gd) and 3 (44 ± 12 at% Ce and 12 ± 5 at% Gd), likely due to a significant amount of GDC being included in the measurement. We do not find significant amounts of La in these regions. The fact that Y signals in regions containing SZO are significantly higher than in parts of the GDC layer without Sr suggests that Y incorporates into SZO when it forms, which should benefit its oxide ion conductivity.

As an aside, we note that certain regions of the GDC—YSZ interface reflect a different chemical environment. Specifically, region J highlighted in Fig. S12 shows significant Gd concentrations at the interface. The lack of Sr signal indicates that SrZrO$_3$ is not forming, but it does appear that Gd is segregating toward the interface, potentially creating Gd-doped ZrO$_2$ in addition to Y-containing YSZ. This phenomenon of Gd segregation will be the subject of a future study.

Discussion

Our results for SrO and SZO suggest the need for distinct engineering strategies to mitigate their possible negative impacts on oxide conductivity in SOECs. SrO forms throughout the cell during operation. As there is no viable strategy to increase bulk SrO conductivity significantly, it will be necessary to limit its formation in devices. Most likely, small SrO precipitates such as those seen in Fig. 7 (region 1) will not disrupt device performance. However, ensuring that thick, continuous SrO layers do not form is essential. It will be critical to confirm that SrO will not form thicker layers after more extended testing times or under different operating conditions.

On the other hand, we have demonstrated that the formation of SZO need not disrupt oxide ion conduction, providing that it is doped
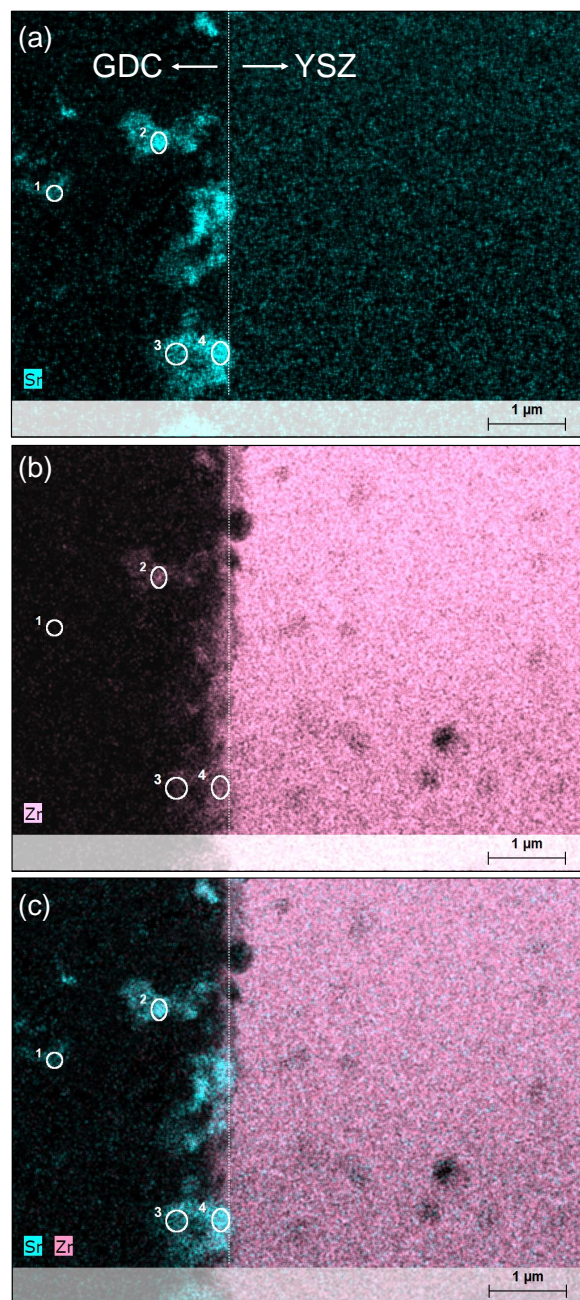
14

Figure 7: Energy Dispersive X-ray Spectroscopy (EDS) maps of (a) Sr (in blue), (b) Zr (in pink), and (c) Sr and Zr together for the boundary region between the Gd-doped CeO_2 (GDC) barrier layer (left) and the YSZ electrolyte (right) in YSZ-based solid-oxide electrolyzer cells. The images were obtained from scanning transmission electron miscroscopy (STEM) images collected after 1000 hours of testing. Regions of interest are circled and labeled in each panel. Quantitative analysis of elemental compositions in the circled regions and other regions of interest are provided in the SI.

with high levels of Y (on the order of 16 at%). While it is known that Y can accompany Zr when SZO forms at the GDC—YSZ interface,[25] targeted engineering strategies may be necessary to increase its concentration. One approach may be to design YSZ electrolytes with higher Y concentrations at the YSZ-GDC interface. Optimal Y concentrations in YSZ are on the order of 20 at% on the Zr site, but designing more Y-rich surfaces may lead to the formation of Y-rich SZO layers during operation without significantly lowering the conductivity of YSZ. At the same time, blocking Ce, Gd, and La diffusion is important, although our EDS analysis suggests that these elements will be present in low concentrations in SZO. It will also be important to block adventitious impurities such as carbon—carbon impurities are electron donors in SZO[44] and will therefore interfere with V_O^{2+} formation.

Another strategy may be to grow a sufficiently Y-doped SZO layer intentionally during synthesis. Given that heavily Y-doped SZO will not limit conductivity, its presence need not be avoided, and intentional growth may reduce resistive losses at disordered interfaces, which Develos-Baraginao *et al.* showed to be the primary source of reduced conductivity across YSZ–SZO–GDC layers.[25] Those authors intentionally synthesized YSZ—SZO heterostructures with small amounts of Y-doping in SZO ($\sim$5 at%). However, they noticed a drop in V_O^{2+} concentrations at the interface due to Y segregation, which may have been due to discrepancies in μ_Y across the heterostructure. Also, in their case, SZO was grown in the orthorhombic crystal structure. Cubic SZO, as is observed in SOECs, may reduce the lattice mismatch, as O–O distances in cubic SZO are more uniform than those in orthorhombic SZO due to octahedral tilting. As a result, it may be possible to design more coherent interfaces, reducing interfacial resistance that commonly arises at heterogeneous interfaces and grain boundaries. However, for this strategy to be most effective, we note that it will also be important to ensure that Sr-rich chemical potentials persist throughout the layer; Zr-rich conditions, which may manifest at the YSZ interface, will

reduce V_O^{2+} concentrations and therefore limit oxide conductivity.

Conclusions

In summary, we have demonstrated that SrO and SZO have distinct effects on oxide ion conductivity in SOECs based on a YSZ electrolyte. Both phases have been observed to form following Sr exsolution from the air electrode, with SrO present throughout the GDC blocking layer, and SZO forming near the GDC—YSZ interface. In SrO, mobile V_O^{2+} defects have poor mobility and high formation energies, leading to a low ionic conductivity that will be detrimental in devices. Doping SrO with other elements that may be present—specifically, Ce, Gd, La, and Y—will reduce conductivity further. As such, avoiding the presence of thick SrO layers in devices is necessary. Further studies should be conducted to confirm that SrO remains relatively disperse for longer operation times more representative of long-term goals for SOEC lifetime.

SZO has a significantly higher oxide conductivity than SrO, but it is still less conductive than YSZ. However, its V_O^{2+} diffusivity is actually on par with that of YSZ, meaning that its main limitation is a low intrinsic V_O^{2+} concentration. Doping SZO with Y offers a promising remedy to this problem by decreasing the formation energy—and increasing the concentration—of V_O^{2+}; conversely, Ce, Gd, and La doping will be harmful. Sufficiently high levels of Y doping (specifically, about 16 at% on the Zr site) will raise the oxide ionic conductivity to levels on par with those of YSZ. Strategies to introduce highly Y-doped SZO layers at the GDC—YSZ interface should limit the material's detrimental effects on oxide conductivity, particularly if resistive losses at interfaces and grain boundaries can be minimized.

Acknowledgments

Associated Content

Supporting Information available: Methodology for SOEC design and characterization of components; AIMD results comparing defect formation in cubic and orthorhombic $SrZrO_3$; phase stability diagram of $SrZrO_3$ and SrO; schematic of cation diffusion in CeO_2; additional defect formation energies and concentration plots for SrO, $SrZrO_3$, and YSZ; calculated binding energies between dopants and oxygen vacancies; and complete STEM-EDS maps of the GDC–YSZ interface, with specific elemental concentrations.

References

(1) Flis, G.; Wakim, G. *Solid Oxide Electrolysis: A Technology Status Assessment*; 2023.

(2) Nechache, A.; Hody, S. Alternative and innovative solid oxide electrolysis cell materials: A short review. *Renew. Sustain. Ener. Rev.* **2021**, *149*, 111322.

(3) Min, G.; Choi, S.; Hong, J. A review of solid oxide steam-electrolysis cell systems: Thermodynamics and thermal integration. *Appl. Energy* **2022**, *328*, 120145.

(4) Goodenough, J. B. Oxide-ion conductors by design. *Nature* **2000**, *404*, 821–823.

(5) Schefold, J.; Brisse, A.; Tietz, F. Nine thousand hours of operation of a solid oxide cell in steam electrolysis mode. *J. Electrochem. Soc.* **2011**, *159*, A137.

(6) Lay-Grindler, E.; Laurencin, J.; Villanova, J.; Cloetens, P.; Bleuet, P.; Mansuy, A.; Mougin, J.; Delette, G. Degradation study by 3D reconstruction of a nickel–yttria stabilized zirconia cathode after high temperature steam electrolysis operation. *J. Power Sources* **2014**, *269*, 927–936.

(7) Kostogloudis, G. C.; Ftikos, C. Properties of A-site-deficient $La_{0.6}Sr_{0.4}Co_{0.2}Fe_{0.8}O_{3-\delta}$-based perovskite oxides. *Solid State Ionics* **1999**, *126*, 143–151.

(8) Liang, M.; Yu, B.; Wen, M.; Chen, J.; Xu, J.; Zhai, Y. Preparation of NiO–YSZ composite powder by a combustion method and its application for cathode of SOEC. *Int. J. Hydrogen Ener.* **2010**, *35*, 2852–2857.

(9) Biswas, S.; Kaur, G.; Paul, G.; Giddey, S. A critical review on cathode materials for steam electrolysis in solid oxide electrolysis. *Int. J. Hydrogen Ener.* **2023**, *48*, 12541–12570.

(10) Ni, M.; Leung, M. K.; Leung, D. Y. Technological development of hydrogen production by solid oxide electrolyzer cell (SOEC). *Int. J Hydrogen Ener.* **2008**, *33*, 2337–2354.

(11) Kiebach, R.; Zhang, W.-W.; Zhang, W.; Chen, M.; Norrman, K.; Wang, H.-J.; Bowen, J. R.; Barfod, R.; Hendriksen, P. V. Stability of $La_{0.6}Sr_{0.4}Co_{0.2}Fe_{0.8}O_3/Ce_{0.9}Gd_{0.1}O_2$ cathodes during sintering and solid oxide fuel cell operation. *J. Power Sources* **2015**, *283*, 151–161.

(12) Laurencin, J.; Hubert, M.; Sanchez, D. F.; Pylypko, S.; Morales, M.; Morata, A.; Morel, B.; Montinaro, D.; Lefebvre-Joud, F.; Siebert, E. Degradation mechanism of $La_{0.6}Sr_{0.4}Co_{0.2}Fe_{0.8}O_{3-\delta}/Gd_{0.1}Ce_{0.9}O_{2-\delta}$ composite electrode operated under solid oxide electrolysis and fuel cell conditions. *Electrochim. Acta* **2017**, *241*, 459–476.

(13) Kim, S. J.; Kim, S. W.; Park, Y. M.; Kim, K. J.; Choi, G. M. Effect of Gd-doped ceria interlayer on the stability of solid oxide electrolysis cell. *Solid State Ionics* **2016**, *295*, 25–31.

(14) Tietz, F.; Sebold, D.; Brisse, A.; Schefold, J. Degradation phenomena in a solid oxide electrolysis cell after 9000 h of operation. *J. Power Sources* **2013**, *223*, 129–135.

(15) The, D.; Grieshammer, S.; Schroeder, M.; Martin, M.; Al Daroukh, M.; Tietz, F.; Schefold, J.; Brisse, A. Microstructural comparison of solid oxide electrolyser cells operated for 6100 h and 9000 h. *J. Power Sources* **2015**, *275*, 901–911.

(16) Chen, K.; Hyodo, J.; Dodd, A.; Ai, N.; Ishihara, T.; Jian, L., et al. Chromium deposition and poisoning of $La_{0.8}Sr_{0.2}MnO_3$ oxygen electrodes of solid oxide electrolysis cells. *Faraday Discuss.* **2015**, *182*, 457–476.

(17) Rinaldi, G.; Nakajo, A.; Burdet, P.; Oveisi, E.; Cantoni, M. Strontium migration at the GDC-YSZ interface of solid oxide cells in SOFC and SOEC modes. *ECS Transactions* **2017**, *78*, 3297.

(18) Bi, J.; Yang, S.; Zhong, S.; Wang, J.-Q.; Fan, C.; Chen, X.; Liu, Y. An insight into the effects of B-site transition metals on the activity, activation effect and stability of perovskite oxygen electrodes for solid oxide electrolysis cells. *J. Power Sources* **2017**, *363*, 470–479.

(19) Niania, M.; Podor, R.; Britton, B.; Skinner, S.; Kilner, J. High temperature and in situ study of SrO surface precipitation on perovskite ceramics. European Microscopy Congress 2016: Proceedings. 2016; pp 834–835.

(20) Rupp, G. M.; Téllez, H.; Druce, J.; Limbeck, A.; Ishihara, T.; Kilner, J.; Fleig, J. Surface chemistry of $La_{0.6}Sr_{0.4}CoO_{3-\delta}$ thin films and its impact on the oxygen surface exchange resistance. *J. Mater. Chem. A* **2015**, *3*, 22759–22769.

(21) Lu, M. Y.; Railsback, J. G.; Wang, H.; Liu, Q.; Chart, Y. A.; Zhang, S.-L.; Barnett, S. A. Stable high current density operation of $La_{0.6}Sr_{0.4}Co_{0.2}Fe_{0.8}O_{3-\delta}$ oxygen electrodes. *J. Mater. Chem. A* **2019**, *7*, 13531–13539.

(22) Wankmüller, F.; Szász, J.; Joos, J.; Wilde, V.; Störmer, H.; Gerthsen, D.; Ivers-Tiffée, E. Correlative tomography at the cathode/electrolyte interfaces of solid oxide fuel cells. *J. Power Sources* **2017**, *360*, 399–408.

(23) Simner, S. P.; Anderson, M. D.; Engelhard, M. H.; Stevenson, J. W. Degradation Mechanisms of La–Sr–Co–Fe–O_3 SOFC Cathodes. *Electrochem. Solid State Lett.* **2006**, *9*, A478.

(24) Lu, Z.; Darvish, S.; Hardy, J.; Templeton, J.; Stevenson, J.; Zhong, Y. $SrZrO_3$

(25) Develos-Bagarinao, K.; Yokokawa, H.; Kishimoto, H.; Ishiyama, T.; Yamaji, K.; Horita, T. Elucidating the origin of oxide ion blocking effects at $GDC/SrZr(Y)O_3/YSZ$ interfaces. *J. Mater. Chem. A* **2017**, *5*, 8733–8743.

(26) Pan, Z.; Liu, Q.; Ni, M.; Lyu, R.; Li, P.; Chan, S. H. Activation and failure mechanism of $La_{0.6}Sr_{0.4}Co_{0.2}Fe_{0.8}O_{3-\delta}$ air electrode in solid oxide electrolyzer cells under high-current electrolysis. *Int. J. Hydrogen Ener.* **2018**, *43*, 5437–5450.

(27) Shen, J.; Miao, B.; Liu, Q.; Wu, Y.; Chan, S. H.; Zhong, Z.; Pan, Z. Activation of LSCF–YSZ interface by cobalt migration during electrolysis operation in solid oxide electrolysis cells. *Int. J. Hydrogen Ener.* **2022**, *47*, 38114–38123.

(28) Chen, K.; Jiang, S. P. Surface segregation in solid oxide cell oxygen electrodes: phenomena, mitigation strategies and electrochemical properties. *Electrochem. Ener. Rev.* **2020**, *3*, 730–765.

(29) Feng, Z.; Hong, W. T.; Fong, D. D.; Lee, Y.-L.; Yacoby, Y.; Morgan, D.; Shao-Horn, Y. Catalytic activity and stability of oxides: the role of near-surface atomic structures and compositions. *Acc. Chem. Res.* **2016**, *49*, 966–973.

(30) Riva, M.; Kubicek, M.; Hao, X.; Franceschi, G.; Gerhold, S.; Schmid, M.; Hutter, H.; Fleig, J.; Franchini, C.; Yildiz, B.; Diebold, U. Influence of surface atomic structure demonstrated on oxygen incorporation mechanism at a model perovskite oxide. *Nat. Commun.* **2018**, *9*, 3710.

(31) Chen, Y.; Bu, Y.; Zhang, Y.; Yan, R.; Dong, D.; Zhao, B.; Yoo, S.; Dang, D.;

Hu, R.; Yang, C.; Liu, M. A highly efficient and robust nanofiber cathode for solid oxide fuel cells. *Adv. Ener. Mater.* **2017**, *7*, 1601890.

(32) Lee, S.; Zhang, W.; Khatkhatay, F.; Jia, Q.; Wang, H.; MacManus-Driscoll, J. L. Strain tuning and strong enhancement of ionic conductivity in $SrZrO_3$–RE_2O_3 (RE = Sm, Eu, Gd, Dy, and Er) nanocomposite films. *Adv. Funct. Mater.* **2015**, *25*, 4328–4333.

(33) Poulsen, F. W.; van der Puil, N. Phase relations and conductivity of Sr-and La-zirconates. *Solid State Ionics* **1992**, *53*, 777–783.

(34) Hohenberg, P.; Kohn, W. Inhomogeneous electron gas. *Phys. Rev.* **1964**, *136*, B864.

(35) Kohn, W.; Sham, L. J. Self-Consistent Equations Including Exchange and Correlation Effects. *Phys. Rev.* **1965**, *140*, A1133–A1138.

(36) Department of Energy Hydrogen and Fuel Cell Technologies Office, Technical Targets for High Temperature Electrolysis. 2022; https://www.energy.gov/eere/fuelcells/technical-targets-high-temperature-electrolysis.

(37) Heyd, J.; Scuseria, G. E.; Ernzerhof, M. Hybrid functionals based on a screened Coulomb potential. *J. Chem. Phys.* **2003**, *118*, 8207–8215.

(38) Heyd, G. E.; Scuseria, J.; Ernzerhof, M. Erratum: "Hybrid functionals based on a screened Coulomb potential"[J. Chem. Phys. 118, 8207 (2003)]. *J. Chem. Phys.* **2006**, *124*, 219906.

(39) Kresse, G.; Furthmüller, J. Efficient iterative schemes for *ab initio* total-energy calculations using a plane-wave basis set. *Phys. Rev. B* **1996**, *54*, 11169.

(40) Perdew, J. P.; Burke, K.; Ernzerhof, M. Generalized Gradient Approximation Made Simple. *Phys. Rev. Lett.* **1996**, *77*, 3865–3868.

(41) Weston, L.; Janotti, A.; Cui, X. Y.; Himmetoglu, B.; Stampfl, C.; Van de Walle, C. G. Structural and electronic properties of $SrZrO_3$ and $Sr(Ti,Zr)O_3$ alloys. *Phys. Rev. B* **2015**, *92*, 085201.

(42) Weston, L.; Janotti, A.; Cui, X.; Stampfl, C.; Van de Walle, C. G. Acceptor doping in the proton conductor $SrZrO_3$. *Phys. Chem. Chem. Phys. 19*, 11485–11491.

(43) Rowberg, A. J. E.; Weston, L.; Van de Walle, C. G. Optimizing proton conductivity in zirconates through defect engineering. *ACS Appl. Ener. Mater.* **2019**, *2*, 2611–2619.

(44) Rowberg, A. J. E.; Swift, M. W.; Van de Walle, C. G. Understanding carbon contamination in the proton-conducting zirconates and cerates. *Phys. Chem. Chem. Phys.* **2021**, *23*, 14205–14211.

(45) Blöchl, P. E. Projector augmented-wave method. *Phys. Rev. B* **1994**, *50*, 17953–17979.

(46) Kresse, G.; Joubert, D. From ultra-soft pseudopotentials to the projector augmented-wave method. *Phys. Rev. B* **1999**, *59*, 1758–1775.

(47) Alaydrus, M.; Sakaue, M.; Kasai, H. A DFT+ U study on the contribution of 4f electrons to oxygen vacancy formation and migration in Ln-doped CeO_2. *Phys. Chem. Chem. Phys.* **2016**, *18*, 12938–12946.

(48) Momma, K.; Izumi, F. VESTA3 for three-dimensional visualization of crystal, volumetric and morphology data. *J. Appl. Crystal.* **2011**, *44*, 1272–1276.

(49) Henkelman, G.; Jónsson, H. Improved tangent estimate in the nudged elastic band method for finding minimum energy paths and saddle points. *J. Chem. Phys.* **2000**, *113*, 9978–9985.

(50) Henkelman, G.; Uberuaga, B. P.; Jónsson, H. A climbing image nudged

elastic band method for finding saddle points and minimum energy paths. *J. Chem. Phys.* **2000**, *113*, 9901–9904.

(51) Freysoldt, C.; Grabowski, B.; Hickel, T.; Neugebauer, J.; Kresse, G.; Janotti, A.; Van de Walle, C. G. First-principles calculations for point defects in solids. *Rev. Mod. Phys.* **2014**, *86*, 253.

(52) Freysoldt, C.; Neugebauer, J.; Van de Walle, C. G. Fully *ab initio* finite-size corrections for charged-defect supercell calculations. *Phys. Rev. Lett.* **2009**, *102*, 016402.

(53) Freysoldt, C.; Neugebauer, J.; Van de Walle, C. G. Electrostatic interactions between charged defects in supercells. *Phys. Status Solidi B* **2011**, *248*, 1067–1076.

(54) Van Zeghbroeck, B. J. *Principles of Semiconductor Devices*; Boulder: University of Colorado, 2011.

(55) Chase Jr, M. W. NIST-JANAF thermochemical tables. *J. Phys. Chem. Ref. Data, Monograph* **1998**, *9*, 1.

(56) French, R. H.; Glass, S. J.; Ohuchi, F. S.; Xu, Y. N.; Ching, W. Y. Experimental and theoretical determination of the electronic structure and optical properties of three phases of ZrO_2. *Phys. Rev. B* **1994**, *49*, 5133–5142.

(57) Rao, A.; Kearney, R. Logarithmic derivative reflectance spectra of BaO and SrO. *Phys. Stat. Sol. B* **1979**, *95*, 243–250.

(58) Kennedy, B. J.; Howard, C. J.; Chakoumakos, B. C. High-temperature phase transitions in $SrZrO_3$. *Phys. Rev. B* **1999**, *59*, 4023.

(59) Zhang, A.; Lü, M.; Wang, S.; Zhou, G.; Wang, S.; Zhou, Y. Novel photoluminescence of $SrZrO_3$ nanocrystals synthesized through a facile combustion method. *J. Alloys Cmpnd.* **2007**, *433*, L7–L11.

(60) Lee, Y.; Lee, J.; Noh, T.; Byun, D. Y.; Yoo, K. S.; Yamaura, K.; Takayama-Muromachi, E. Systematic trends in the electronic structure parameters of the 4d transition-metal oxides $SrMO_3$ (M= Zr, Mo, Ru, and Rh). *Phys. Rev. B* **2003**, *67*, 113101.

(61) Matsuda, T.; Yamanaka, S.; Kurosaki, K.; Kobayashi, S.-i. High temperature phase transitions of $SrZrO_3$. *J. Alloys Cmpnds.* **2003**, *351*, 43–46.

(62) de Ligny, D.; Richet, P. High-temperature heat capacity and thermal expansion of $SrTiO_3$ and $SrZrO_3$ perovskites. *Phys. Rev. B* **1996**, *53*, 3013–3022.

(63) Wang, Y.; Cai, C.; Li, L.; Yang, L.; Zhou, Y.; Zhou, G. Oxygen vacancy ordering induced displacements of cations in yttria-stabilized zirconia. *AIP Adv.* **2016**, *6*, 095113.

(64) Bogicevic, A.; Wolverton, C.; Crosbie, G. M.; Stechel, E. B. Defect ordering in aliovalently doped cubic zirconia from first principles. *Phys. Rev. B* **2001**, *64*, 014106.

(65) Kilo, M.; Argirusis, C.; Borchardt, G.; Jackson, R. A. Oxygen diffusion in yttria stabilised zirconia—experimental results and molecular dynamics calculations. *Phys. Chem. Chem. Phys.* **2003**, *5*, 2219–2224.

(66) Kushima, A.; Yildiz, B. Oxygen ion diffusivity in strained yttria stabilized zirconia: where is the fastest strain? *J. Mater. Chem.* **2010**, *20*, 4809–4819.

(67) Lide, D. R. CRC handbook of chemistry and physics. *12J204* **2012**,

(68) Huntelaar, M.; Booij, A.; Cordfunke, E. The standard molar enthalpies of formation of $BaZrO_3$(s) and $SrZrO_3$(s). *J. Chem. Thermodyn.* **1994**, *26*, 1095 – 1101.

(69) Konings, R. J.; Beneš, O.; Kovács, A.; Manara, D.; Sedmidubský, D.;

Gorokhov, L.; Iorish, V. S.; Yungman, V.; Shenyavskaya, E.; Osina, E. The thermodynamic properties of the f-elements and their compounds. Part 2. The lanthanide and actinide oxides. *J. Phys. Chem. Ref. Data* **2014**, *43*.

(70) Limpijumnong, S.; Van de Walle, C. G. Diffusivity of native defects in GaN. *Phys. Rev. B* **2004**, *69*, 035207.

(71) Guo, Z.; Zhu, L.; Zhou, J.; Sun, Z. Design principles of tuning oxygen vacancy diffusion in $SrZrO_3$ for resistance random access memory. *J. Mater. Chem. C* **2015**, *3*, 4081–4085.

(72) Kreuer, K.-D. Proton-conducting oxides. *Annu. Rev. Mater. Res.* **2003**, *33*, 333–359.

(73) Labrincha, J.; Frade, J.; Marques, F. Defect structure of $SrZrO_3$. *Solid State Ionics* **1993**, *61*, 71–75.

(74) Beschnitt, S.; Zacherle, T.; De Souza, R. A. Computational study of cation diffusion in ceria. *J. Phys. Chem. C* **2015**, *119*, 27307–27315.

(75) Körfer, S.; Bonkowski, A.; Kler, J.; Hatton, P.; Uberuaga, B. P.; De Souza, R. A. The sluggish diffusion of cations in CeO_2 probed through molecular dynamics and metadynamics simulations. *Adv. Eng. Mater.* **2023**,

(76) Vineyard, G. H. Frequency factors and isotope effects in solid state rate processes. *J. Phys. Chem. Solids* **1957**, *3*, 121–127.

(77) Maier, J. *Physical chemistry of ionic materials: ions and electrons in solids*; John Wiley & Sons, 2004.

(78) Labrincha, J.; Marques, F.; Frade, J. Protonic and oxygen-ion conduction in $SrZrO_3$-based materials. *J. Mater. Sci.* **1995**, *30*, 2785–2792.

(79) Ahamer, C.; Opitz, A. K.; Rupp, G.; Fleig, J. Revisiting the temperature dependent ionic conductivity of yttria stabilized zirconia (YSZ). *J. Electrochem. Soc.* **2017**, *164*, F790.